Construction and Building Materials 404 (2023) 133259

Contents lists available at ScienceDirect

Construction and Building Materials

journal homepage: www.elsevier.com/locate/conbuildmat

Long-term field monitoring of slabs-on-ground reinforced with GFRP bars

Mohammed Fasil [a], Muhammad Kalimur Rahman [b,*], Mesfer M. Al-Zahrani [a,b], Antonio Nanni [c], Mohammed A. Al-Osta [a,b], Sami A. Al-Ghamdi [d], Mohammed Al Mehthel [d]

[a] Civil and Environmental Engineering Department, King Fahd University of Petroleum and Minerals (KFUPM), Dhahran, Saudi Arabia
[b] Interdisciplinary Research Center for Construction and Building Materials (IRC-CBM), KFUPM, Dhahran, Saudi Arabia
[c] Department of Civil and Architectural Engineering, University of Miami, Coral Gables, FL, USA
[d] Consulting Services Department, Saudi Aramco, Dhahran, Saudi Arabia

ARTICLE INFO

Keywords:
Glass-fiber reinforced polymer (GFRP) bars
Slabs-on-ground
Ambient exposure
Shrinkage strains
Crack width

ABSTRACT

The current design of GFRP bar-reinforced slabs-on-ground, according to ACI 440.1R-15 is based on an empirical equation derived from the design of steel-reinforced concrete slabs-on-ground, developed based on the subgrade drag equation proposed in Portland Cement Association code (1990). ACI 440.1R-15 explicitly stipulates that field performance data from the application of FRP bar-reinforced slabs-on-ground is required to validate the equation. This paper reports the experimental outcomes of a comprehensive study on the long-term field monitoring of eight large-scale slab-on-ground specimens. Slabs of plan dimensions 6000 × 1100 mm^2, resting on a lean concrete subbase over a compacted soil subgrade and exposed to harsh ambient environment, were monitored for 525 days to study rebar and concrete strain development and concrete cracking. The exposed ambient environment was characterized by averages of 41.7 ℃ with RH 12.8% in summer and 9.5 ℃ with RH 87.7% in winter. The major parameters of the study are reinforcement types (ribbed GFRP, sand-coated GFRP, and ribbed steel), reinforcement spacings (200 mm and 300 mm), slab thicknesses (100 mm and 200 mm), and the presence of a contraction joint. It was observed that all GFRP bar-reinforced slabs developed a transverse mid-panel shrinkage crack within the first 18 days of casting. The maximum average crack widths over the long-term were within the ACI 440.1R-15 and AASHTO LRFD code limit of 0.7 mm, and the maximum strains in rebars in the vicinity of the cracks did not exceed 12.4% of the ultimate strains of the bars. Decreasing the slab thickness from 200 mm to 100 mm did not affect the development of cracking or strain evolution. The presence of a saw-cut contraction was effective in localizing the cracking location.

1. Introduction

Reinforced concrete (RC) structures such as slabs-on-ground, foundation slabs, industrial floors, and deck slabs are characterized by their relatively large surface-to-volume ratio, as compared to beams and columns. As a result, factors such as low early-age tensile strength and shrinkage are conducive to the development of cracks in concrete at an early age [1,2]. The interaction between concrete shrinkage and volumetric instability due to the interaction between concrete shrinkage and internal and external restraints is the dominant factor [3]. Some examples of internal restraints are reinforcing bars and aggregates, while external restraints include slab-subgrade friction, boundary conditions, and loads [4]. When the elastic strains developed in concrete in the slab exceed the tensile strain capacity of concrete, cracks develop to relieve the built-up of stresses [5].

In conventional steel-RC structures, these cracks create a path for the easy penetration of water and aggressive species, resulting in the corrosion of the steel rebars [6]. Corrosion leads to the formation of expansive corrosion products generating tensile stresses in concrete. When these tensile stresses exceed the tensile capacity of the concrete, extensive cracking occurs, degrading the aesthetics and structural performance of RC members [7]. Cracking in steel-RC structures poses major durability issues compromising the structural integrity and creating economic issues such as high maintenance and repair costs.

The corrosion-free and high-strength glass fiber-reinforced polymer (GFRP) bars have gained popularity in both research and field applications in recent years [8], due to remarkable improvements in terms of strength, cost, and durability. With the development of building codes such as ACI 440.11-22 [9], GFRP bars are now considered to be a potential replacement for conventional steel bars, especially in harsh

* Corresponding author.
E-mail address: mkrahman@kfupm.edu.sa (M. Kalimur Rahman).

https://doi.org/10.1016/j.conbuildmat.2023.133259
Received 7 September 2022; Received in revised form 26 June 2023; Accepted 5 September 2023
Available online 12 September 2023

environments where structures are in direct contact with soil and water. The application of GFRP bars in slabs-on-ground eliminates the development of corrosion-induced cracks and thereby prolongs the service life of structures with minimal life-cycle costs.

Several research works reported in the literature have explored the effect of restrained shrinkage on ground-supported slabs, suspended slabs, deck slabs, and concrete pavements reinforced with steel and GFRP bars. End and base-restrained large-scale steel-reinforced concrete slabs undergoing shrinkage in an environmental chamber were monitored for 600 days by Shadravan et al. [4] to investigate the dimensional change response of four types of concrete used in the study. The evolution of shrinkage strains and crack openings was monitored with strain gauges installed at the mid and quarter-spans of all seven specimens. A transverse steel truss provided the longitudinal restraint, while rebars provided the internal restraints. Ghatefar et al. [8,10] studied early-age shrinkage cracks developed in bridge deck slabs with dimensions of 2.5 × 0.765 × 0.18 m^3, which were subjected to laboratory and cyclic environmental conditions such as drying and wetting, and freezing and thawing. The lower elastic modulus of GFRP bars resulted in the development of higher crack widths and rebar strains, as compared to steel bar-reinforced concrete specimens. However, the same factor resulted in the larger crack spacing. The study revealed that the minimum reinforcement ratio proposed by CAN/CSA S6-06 [11] was conservative in the laboratory test conditions used in the study. Shafei et al. [12] conducted field investigations to evaluate the performance of GFRP bar-reinforced bridge deck slabs through live load field tests during early age and long-term monitoring for up to 748 days. In the first three years of monitoring reported in the study, the deck behavior remained consistent and met design specifications satisfactorily. Deck slabs near the abutments were found to have more cracks as compared to the remaining parts of the bridge. Cracks grew rapidly in the first year, but no significant new cracks formed in the subsequent two years, as also seen in steel-reinforced bridge deck slabs. Life-cycle cost analyses confirmed that the application of GFRP bars was more economical, as compared to steel, despite higher initial costs.

A comparative study between three steel-reinforced bridges in Montana, USA was conducted by Cuelho et al. [13] to monitor concrete strains in short-term under live load tests, and long-term from shrinkage and temperature variations, besides distress monitoring and corrosion tests. Monitoring of the three bridges revealed that the decks exhibited linear-elastic behavior under live loads, and no signs of concrete cracking were observed in the process. Pantelides et al. [14] conducted long-term monitoring of concrete strains, bridge displacements, and girder accelerations in precast concrete panels in bridge decks reinforced with GFRP bars in Utah, USA, for two years. The study revealed that the structural behavior was satisfactory and the use of GFRP was expected to extend the service life by 55 years. The GFRP bar-reinforced panels exhibited no signs of concrete cracking and stayed within the design limits for stresses and deflections, and demonstrated successful long-term functionality. Modifications to the bridge deck design to account for the use of GFRP bars effectively prevented deck cracking and maintained small service load deflections throughout the monitoring period.

Kušnírová and Priganc [15] conducted long-term shrinkage monitoring of GFRP and steel-reinforced concrete slabs of dimensions 1800 × 600 × 120 mm^3, and reinforcement ratios varying from 0.3% to 0.5%. To minimize the effect of self-weight and to enable uniform shrinkage, the specimens were placed vertically in an isolation chamber, which prevented sudden variations in temperature and humidity. The study revealed that the steel-reinforced slabs exhibited approximately twice the deflection of the GFRP bar-reinforced slabs, at a given reinforcement ratio. Sonnenschein et al. [16] conducted a study to compare the effect of GFRP and steel reinforcements on the onset of early-age cracking in thermally isolated end-restrained reinforced concrete slabs with overall dimensions of 5300 × 1000 × 300 mm^3. The study revealed that the GFRP bar-reinforced slabs were characterized by small crack spacings and higher crack widths, as compared to their steel-reinforced counterparts.

After a review of the relevant works in the field of restrained shrinkage of concrete elements [4,8,10,12–16], there is, to the best of the authors' knowledge, limited research on the behavior of base-restrained large-scale GFRP bar-reinforced slabs-on-ground in the field. Also, ACI-440.1R-15[17] explicitly mentions that there is a lack of experimental data from the field to verify the design equations provided in the design guide for slabs-on-ground. This paper presents a research in which eight large-scale reinforced concrete slabs-on-ground were monitored in the field over an extended period. The slabs used three types of reinforcements, namely ribbed GFRP bars (PG), sand-coated GFRP bars (GG), and conventional ribbed steel bars (S). The slab specimens cast on a lean concrete base were exposed to the harsh ambient environment for 525 days. Due to drying shrinkage and temperature variations, crack development, crack widths, crack spacing, strains in the concrete, and strains in the reinforcing bars were measured at various locations. This study was conducted as part of the investigation of the 21.3 km-long flood-water mitigation channel in Jazan, Saudi Arabia, which is the largest GFRP bar-reinforced structure in the world [18,19].

2. Experimental program

2.1. Materials

The full-scale slabs of this experimental program were constructed using a concrete mix with 28-days compressive strength of 40.8 MPa (Table 1). The elastic modulus of concrete, E_c was calculated to be 29.8 GPa. Based on the tensile strength of 3.1 MPa, the concrete cracking strain in tension (ε_{ct}) was calculated to be 104 με. Two types of #4 GFRP bars, namely ribbed GFRP (PG) and sand-coated GFRP (GG), and 12.7 mm dia. conventional ribbed steel (S) bars were used as internal reinforcement (Fig. 1). The mechanical properties of the reinforcing bars as experimentally determined are summarized in Table 2. All GFRP reinforcing bars used in the study were samples taken from the flood mitigation channel construction site in Jazan, Saudi Arabia.

2.2. Test specimens and exposure

2.2.1. Large-scale specimens

Eight slabs of plan dimensions of 6000 × 1100 mm^2, with 200 mm and 100 mm thicknesses were constructed for the experimental program. The slab specimens were cast on a 100 mm-thick lean concrete subbase resting on a compacted sand subgrade layer, in a dedicated field station with ample exposure to ambient environment. Variations in ambient temperature and relative humidity were recorded using a weather station, as shown in Fig. 2 (a). The graphs in Fig. 2 (b) show the measured temperature and relative humidity (RH) variations during the monitoring period. The slabs were cast during the coldest days of the year, when the 1-day moving average temperature was 19.2 °C with a high of 26.4 °C and a low of 14.3 °C, and the 1-day moving average RH was 66.2% with a high of 91.5% and a low value of 28.8%. The average temperature and RH were 9.5 °C and 87.7% in winter and 41.7 °C and 12.8% in summer, respectively.

All sections of the 21.3 km-long Jazan floodwater mitigation channel have a 200 mm-thick bottom slab with GFRP bars placed at a depth of 75 mm at a center-to-center spacing of 200 mm [18]. Considering this, two values of rebar spacings were chosen for the study to investigate the effects of reinforcement ratio on the development of crack width. The variables of the study were: (i) rebar types, including ribbed GFRP bars (PG), sand-coated GFRP bars (GG), and steel bars (S); (ii) rebar spacings of 200 mm and 300 mm center-to-center; (iii) slab thicknesses of 100 mm and 200 mm; and (iv) a 6 mm-wide and 12 mm-deep saw-cut contraction joint at midspan. The details of the slabs investigated in the experimental program are shown in Table 3, while schematic details

Table 1
Concrete mix design and strength.

Cement type and content	Aggregates (kg/m^3)			Admixtures (ml /m^3)		Mixing water (l/m^3)	28-day compressive strength (MPa)	
	20 mm	10 mm	Fine	PC 314*	D10*		Comp.	Tens.
Sulfate resisting cement (320 kg/m^3)	770	330	760	1300	2000	160	40.2	3.1

Note: *PC314: Fluidum PC314 high efficiency liquid superplasticizer; Arcrete D10: water reducer & set retarder.

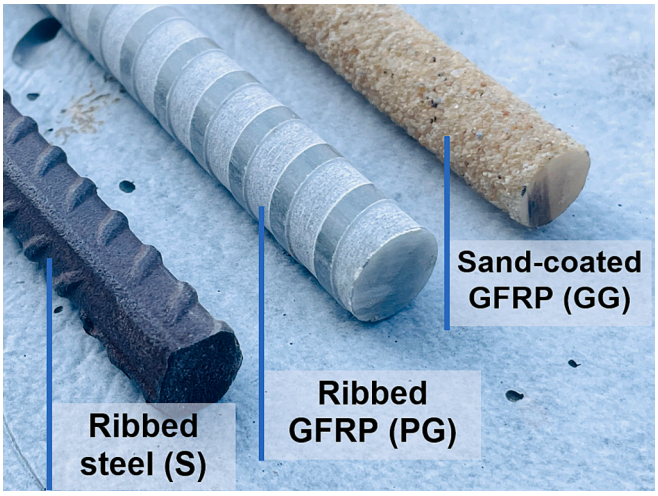

Fig. 1. Reinforcing bars used in the study.

Table 2
Rebars: mechanical properties and dimensions.

Property	Ribbed GFRP (PG)	Sand-coated GFRP (GG)	Conventional ribbed steel (S)
Guaranteed tensile strength (MPa)*	870.9	900.2	584 (yield)
Young's Modulus (GPa)	48.4	43.9	209
Diameter (mm)	13.7	13.5	12.7

Note: *Guaranteed tensile strength: Average tensile strength – thrice the standard deviation of its tensile strength.

are shown in Fig. 3 (a and b).

Fig. 3 (c to f) shows the steps involved in the preparation of the slabs. Molds fabricated using plywood panels were erected and nailed down to the lean concrete base. The rebar mats were placed in the intended position with spacers made of PVC pipes. Rectangular PVC ducts were placed between the formworks of the slabs through which the lead wires from the strain gauges were laid to reach the data logger in the monitoring cabin. Monitoring of the slabs began one day after casting, while the specimens were moist-cured using a double layer of burlap and polyethylene sheets to prevent moisture from escaping to the atmosphere. The moist curing continued until the 6th day after casting. After demolding, the slabs-on-ground were left exposed to the ambient environment.

2.3. Instrumentation and field monitoring

Strain gauges were placed at several points in the slabs to monitor the variation of strains in concrete and reinforcing bars. Strains in the rebars at mid-span, quarter-spans, and ends were monitored using strain gauges (TML FLAB-6–350) as shown in Fig. 4 (a). Embedded strain gauges (TML PMFL-60) were placed in the concrete at the level of the reinforcement and 50 mm from the subbase (Fig. 4 (b)). Fig. 4 (c) shows the strain gauges in a typical slab, with lead wires passing through PVC channels to reach the data acquisition systems (Fig. 4 (d)). The strain gauges embedded in the concrete were placed at different depths to monitor the shrinkage strains across the depth. Details of labels and locations of the strain gauges installed in rebars and concrete are

Table 3
Test matrix of the large-scale slab-on-ground specimens.

Slab No.	Specimen Name	Rebar type	Slab thickness	Spacing
1	PG-200	Ribbed GFRP (PG)	200	200
2	PG-300			300
3	PG-200-H[§]		100	200
4	PG-200-SC*		200	200
5	GG-200	Sand-coated GFRP	200	200
6	GG-300	(GG)		300
7	S-200	Ribbed Steel (S)		200
8	PL	Nil		N/A

Note: [§]'H' indicates half-thickness slab; *Only PG-200-SC has a saw-cut 6 mm × 12 mm to study the effect of a saw-cut joint on cracking.

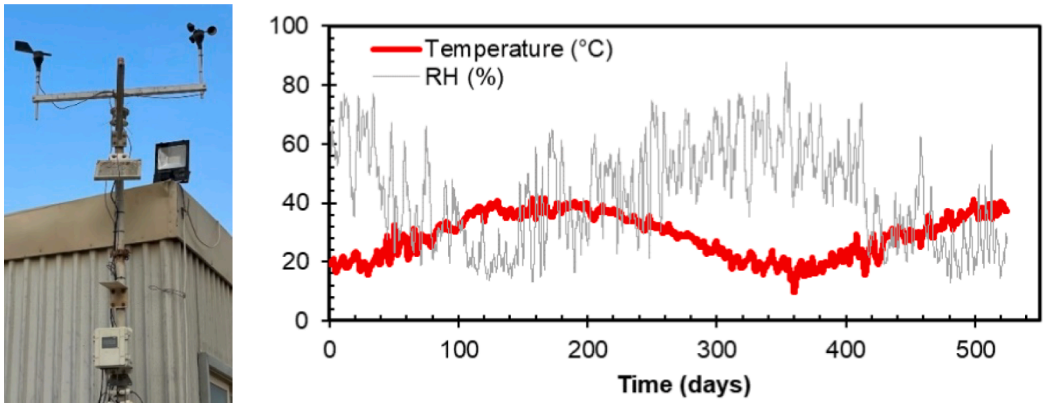

(a) weather station (b) temperature and RH time-history

Fig. 2. Weather station: measurement of temperature and relative humidity (1-day moving average).

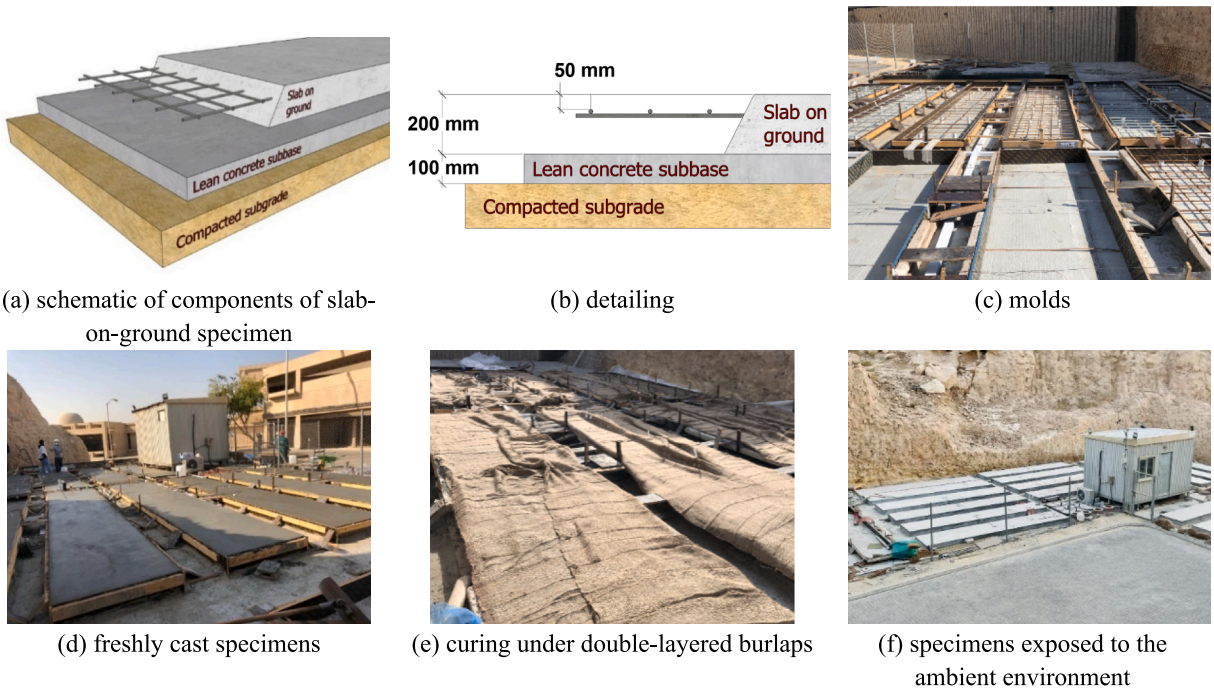

(a) schematic of components of slab-on-ground specimen

(b) detailing

(c) molds

(d) freshly cast specimens

(e) curing under double-layered burlaps

(f) specimens exposed to the ambient environment

Fig. 3. Slab-on-ground specimens.

illustrated in Fig. 4 (e and f).

Measurements from 65 strain gauges were recorded for 525 days at five-minute intervals and stored in the internal memory of the data logger, shown in Fig. 4 (d). A HOBO U30 weather station (Fig. 2 (a)) was set up on-site to monitor ambient temperature, relative humidity, wind speeds, gust speeds, and wind direction.

An interactive computer application called SHEVOL (Shrinkage Evolution) was developed using MATLAB to plot the evolution of strains from various sensors and for comparisons (Fig. 5). The development of cracks in the specimens, their width, and their evolution were physically monitored while the onset of cracking was assessed from the live strain evolution curves in SHEVOL.

3. Results and discussion

3.1. Crack distribution and crack widths in slabs

3.1.1. Crack mapping

After casting the slabs, crack mapping of all slabs-on-ground was performed at regular intervals. Central or near-center cracks developed in all slabs at the ages shown in Table 4. The cracks, as they developed, were observed in SHEVOL from the sensors two to four days before they were visually observed on the surface of the slabs, as shown in Table 4. On the surface, a thin crack initially formed at the center of the slab (Fig. 6), increasing in width with time and progressing downwards. The central crack was associated with smaller cracks on the surface of some slabs, which developed at quarter points and other locations at later times. The crack widths and their distribution at day 525 are shown in Fig. 6 (a to h).

All slabs reinforced with ribbed GFRP (PG) and sand-coated GFRP (GG) bars spaced at 200 mm and 300 mm generally developed a central full-depth transverse crack, with or without minor cracks on either side of the central crack. In contrast, the steel-reinforced slab (S-200) did not exhibit any major cracks except for a few thin transverse cracks and one longitudinal crack (<0.01 mm) that were all randomly scattered. The plain concrete slab (PL) developed a central full-depth crack with an average crack width of 0.79 mm. This indicates that the presence of rebar and its elastic modulus had a significant effect on the nature of cracks developed in the slab.

PG-200-SC, the GFRP-bar reinforced slab with a central 6 mm wide × 12 mm deep saw-cut contraction joint, exhibited no cracks on either side, except for a 0.43 mm wide crack that developed at the joint, as expected. PG-200-H, the 100 mm-thick slab with GFRP bars developed a central full-depth crack with an average width of 0.61 mm.

3.1.2. Effect of reinforcement types and spacings

A comparison of crack widths of GFRP bar-reinforced slabs of different types (PG and GG) and the plain slab is shown in Table 4. The sand-coated GFRP (GG) bar was generally found to be more effective in controlling the crack widths than the ribbed GFRP (PG) bars at smaller spacing, probably due to a better bond strength in GG bars, as compared to PG bars. At a spacing of 200 mm, the average crack width in slab GG-200 was 17.7% less than that of slab PG-200. However, at a spacing of 300 mm, the average crack width in slab GG-300 was very close to that of slab PG-300. The unreinforced concrete slab (PL) showed the highest crack widths among the eight slabs monitored in this study, with an average crack width of 0.79 mm.

A lower bar spacing, which corresponds to a higher reinforcement ratio provides higher restraint and distributes the cracks over the length of the slab, resulting in smaller crack widths. A 6.5% higher crack width was observed for slab PG-300 compared to the PG-200 slab. Similarly, GG-300 was found to have a 29.4% higher crack width, when compared to the GG-200 specimen. In summary, the average crack widths in GFRP bar-reinforced slabs were within the ACI 440.1R-15 [17] and AASHTO LRFD [28] allowable crack width limit of 0.7 mm, as shown in Fig. 7.

3.1.3. Effect of slab thickness and saw-cut contraction joint

A comparison between slabs PG-200 and PG-200-H (100 mm-thick) to investigate the effect of slab thickness on the crack width showed no significant difference, as both slabs had an average crack width of 0.62 mm. In the case of PG-200-SC, the crack initiated only at the joint, exhibiting a much better aesthetic appearance since the crack developed within the joint created. The average crack width at the joint was 0.43 mm, 30.6% less than at PG-200, and the cracks developed at approximately the same time in the two slabs. Thus, in GFRP bar-reinforced slabs-on-ground, the provision of a saw-cut contraction joint to

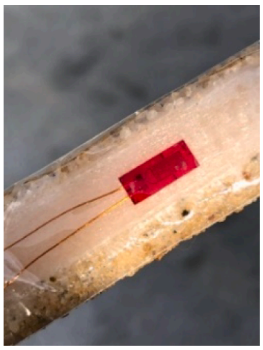

(a) Rebar strain gauge

(b) Concrete-embedded strain gauge

(c) Instrumented slabs

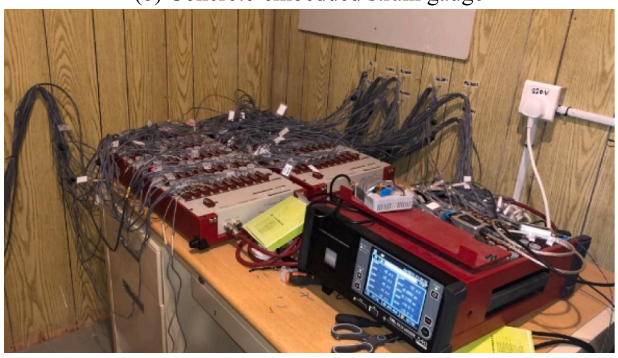

(d) Data acquisition systems

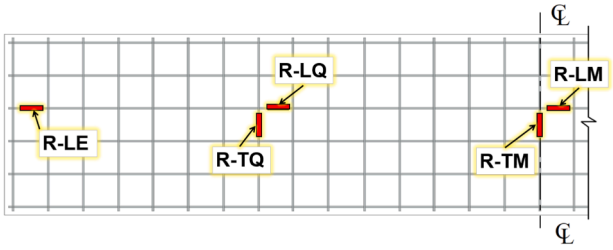

Note: R = rebar strain gauge; Locations: M = midspan; Q = quarter-span; E = end; L = longitudinal; T = transverse

(e) Location of rebar strain gauges

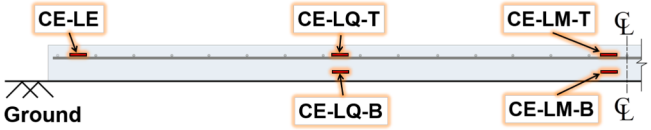

Note: CE = concrete embedded strain gauge; Locations: M = midspan; Q = quarter-span; E = end; L = longitudinal; T = 50 mm from top surface (rebar-level); B = 50 mm from base (ground)

(f) Location of concrete-embedded strain gauges

Fig. 4. Instrumentation of slabs.

contain the crack within the cut would result in a surface free from random cracks.

3.2. Reinforcement and concrete strains

The evolution of strains in the concrete and reinforcing bars were monitored in the slab-on-ground specimens shortly after the initial setting of the concrete from the day of casting. Both early-age and long-term evolution of strains (one-day moving average) were analyzed.

The effects of daily and seasonal temperature variations on the evolution of rebar and concrete strains in a typical specimen (i.e., PG-200) are shown in Fig. 8. Fig. 8 (a) shows the short-term behavior (up to 21 days) of rebar strains at the gauge locations R-LM (midspan) and R-LQ (quarter-span). The solid lines of R-LM and R-LQ are the actual field reading, while the dashed lines plot their corresponding 1-day moving average. The blue dotted lines in Fig. 8 show the actual temperature readings.

The positive strains in the longitudinal bar in the PG-200 slab shot up rapidly at R-LM (mid-span), indicating the development of a crack in concrete at this location. While at R-LQ (quarter-span), the strain readings indicated expansion for approximately 5 days, followed by increasing negative total strains indicating contraction. The effect of seasonal temperature variation on concrete strains in slab PG-200 at two locations (mid-span: CE-LM-T and quarter-span: CE-LQ-T) at the rebar level is shown in Fig. 8 (b). Large variations in the measured strains were observed corresponding to the variations in the ambient temperature. The measured total strains indicate increasing contraction (negative strain) in concrete as the temperature increased during summer, which

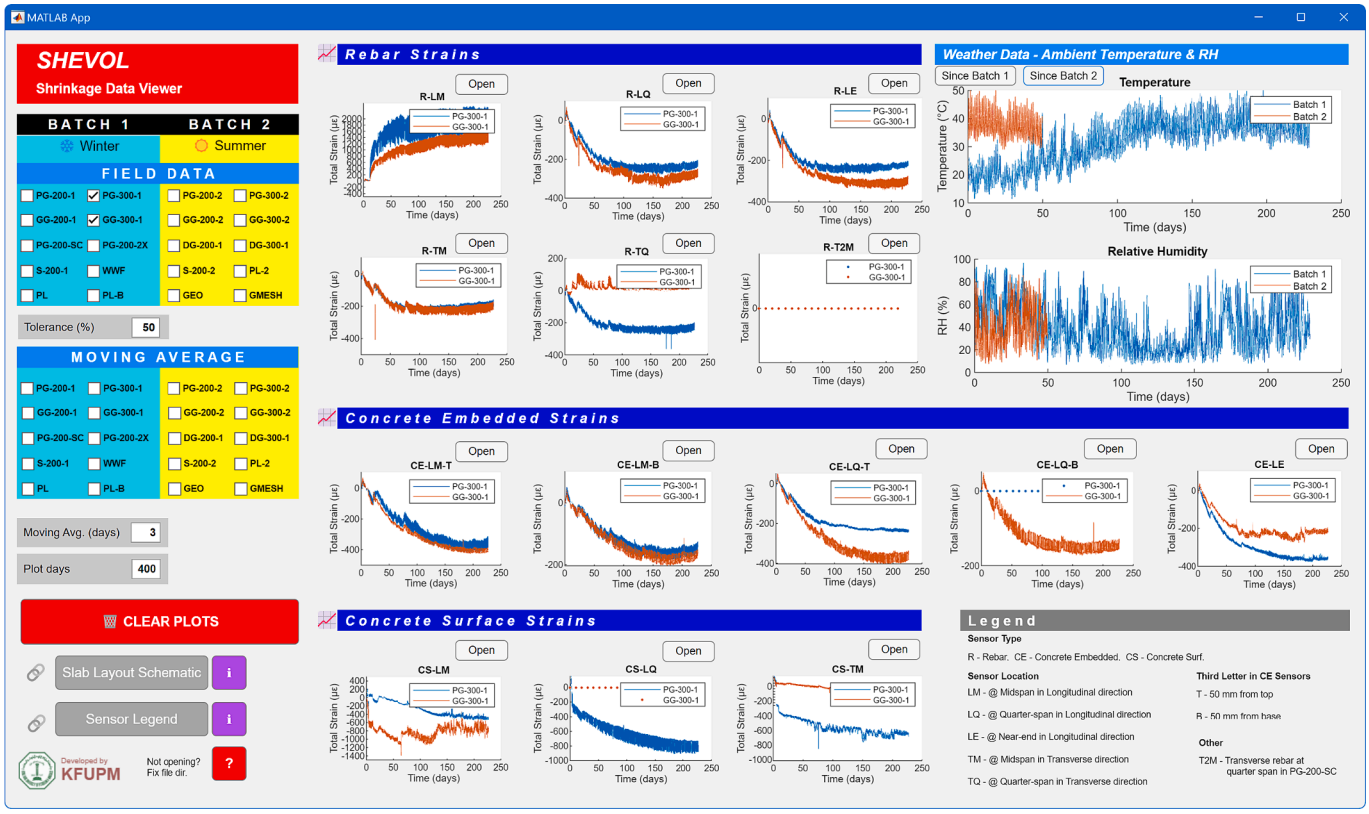

Fig. 5. Shrinkage data viewer application (SHEVOL).

Table 4
Crack characteristics of slab specimens.

Slab No.	Slab	Location of main crack	Days to first crack		Average crack width (mm)	Crack depth
			Visually observed	Detected by sensors		
1	PG-200	Central	13	9	0.62	Full-depth
2	PG-300	Central	13	11	0.66	Full-depth
3	PG-200-H	Central	12	10	0.61	Full-depth
4	PG-200-SC	Within joint	13	10	0.43	Full-depth
5	GG-200	Central	20	18	0.51	Full-depth
6	GG-300	Central	14	12	0.66	Full-depth
7	S-200	Nil	–	–	–	No full-depth cracks
8	PL	Central	12	–	0.79	Full-depth

reversed as the temperature decreased. A sketch summarizing the nomenclature of monitoring points, variables, and slab comparisons presented in the discussion on results are shown in Fig. 9.

3.3. *Effect of rebar type and spacing on strain evolution in bars*

The evolution of strains in the reinforcement of slabs PG-200, PG-200, GG-200, GG-300, and S-200 is plotted in Fig. 10. The effect of reinforcement type and spacing on the evolution of strains in the reinforcement and the onset of cracking in the slabs are presented below.

3.3.1. *Evolution of rebar strains in the central longitudinal bar at midspan (R-LM)*

(i) Slabs PG-200, GG-200, and S-200

The early-age strain response at R-LM of PG-200, GG-200, and S-200 (Fig. 10 (a)) shows tensile strains in the bars owing to the swelling of the surrounding concrete in the first three days after casting. This swelling of the concrete is attributed to the cumulative effect of the chemical and physical properties of the cement, moisture distribution in the pore structure of the concrete leading to autogenous expansion, and the formation of hydration products with larger volumes [20–23]. This swelling was followed by a decrease in strain in all three slabs. Both GFRP bar-reinforced slabs PG-200 and GG-200 exhibited a steep rise in the tensile strain within the first 20 days, indicating the development of concrete drying shrinkage cracks near the strain gauges. This steep rise occurred on the 9^{th} and 18^{th} days in PG-200 and GG-200, respectively, causing the rebars to be in a state of tensile stress. The cracking in these slabs can be seen in the crack maps in Fig. 6. R-LM in the steel reinforced slab, S-200, continued to show compressive strains until the 115^{th} day, beyond which the development of tensile strains was noted. The peak R-LM strains in the slabs were found to be 1,950 $\mu\varepsilon$, 2,339 $\mu\varepsilon$, and 953 $\mu\varepsilon$ in PG-200, GG-200, and S-200 slab specimens, respectively. Tensile strains in R-LM peaked on approximately the 250^{th} day during the summer season, falling to a lower value near the 350^{th} day (peak of winter) and then increasing again to the previous value in summer.

(ii) Slabs PG-300 and GG-300

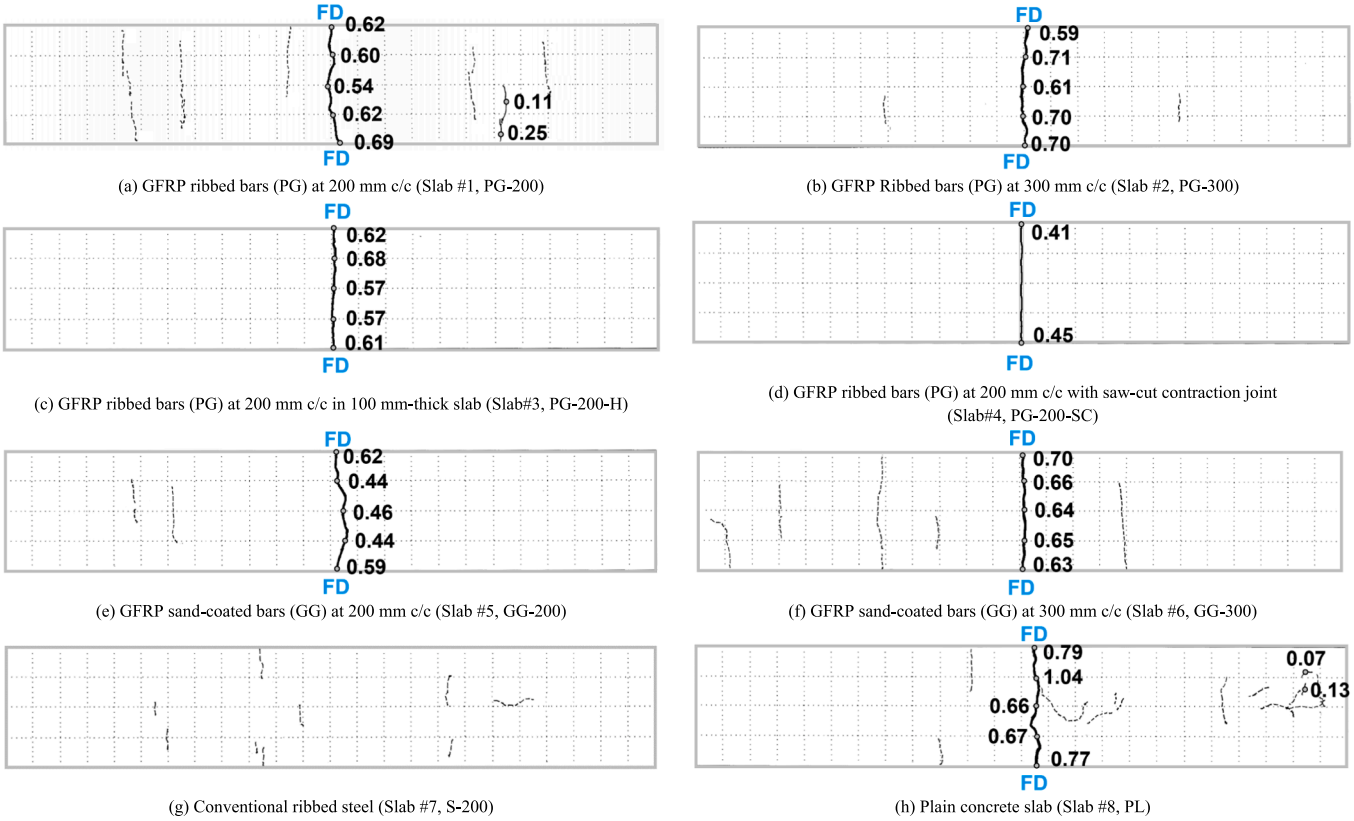

Fig. 6. Crack mapping of slab-on-ground specimens (top surface) (**FD** indicates full-depth crack; solid lines indicate crack width >0.01 mm; dashed lines indicate crack widths <0.01 mm; and dotted line indicates grid lines).

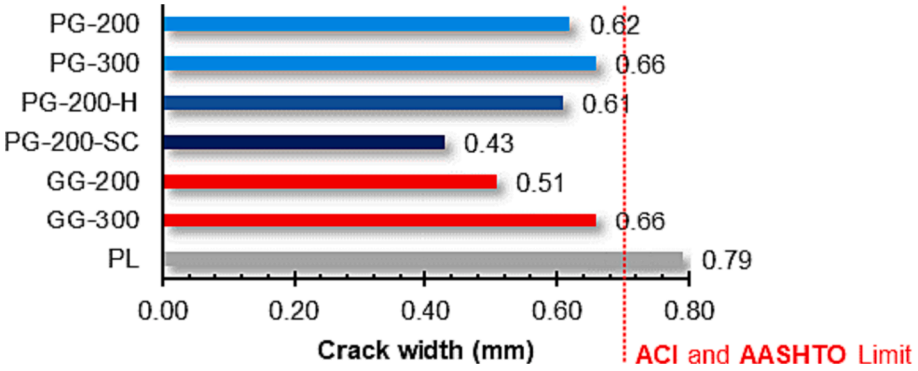

Fig. 7. Crack width: effect of reinforcement type and spacing.

The onset of central prominent drying shrinkage crack was noted in PG-300 and GG-300 on days 11 and 12, respectively, as indicated by an abrupt increase in R-LM strains. The long-term response shows the highest strains of 2,228 με and 1,524 με in PG-300 and GG-300, respectively. Although the tensile strain developed in the rebar is a function of the location of the sensor with respect to the position of the crack, the larger strain in PG-300 could be attributed to the larger crack width near the sensor R-LM compared to the corresponding crack width in GG-300.

(iii) Slabs PG-200 and PG-300

Low tensile strains developed in the early hours in the GFRP bars in slabs PG-200 and PG-300, and then a jump in the tensile strain on the 9th and 11th days, respectively, indicates the development of drying shrinkage crack at a nearby location, as shown in the crack maps in Fig. 6 (a and b). The tensile strain evolution curve in the GFRP bars in both PG-200 and PG-300 followed the same path up to the 35th day. Later, PG-300 (2,228 με) exhibited higher strains compared to PG-200 (1,950 με), which could be attributed to the lesser internal restraints due to the lower reinforcement ratio and the resulting larger crack width, as shown in the crack maps (Fig. 6).

(iv) Slabs GG-200 and GG-300

The development of cracking in the slabs GG-200 and GG-300 was observed on the 18th and 12th days, respectively, as inferred from the sudden increase in tensile strain in the GFRP bars at R-LM. At the peak of summer, the highest strains in the slabs GG-200 and GG-300 were 2,339 με and 1,524 με, respectively.

Comparing the strain evolution in sensors R-LM in PG-200 and PG-300, the slab with the larger reinforcement ratio, GG-200, had a larger

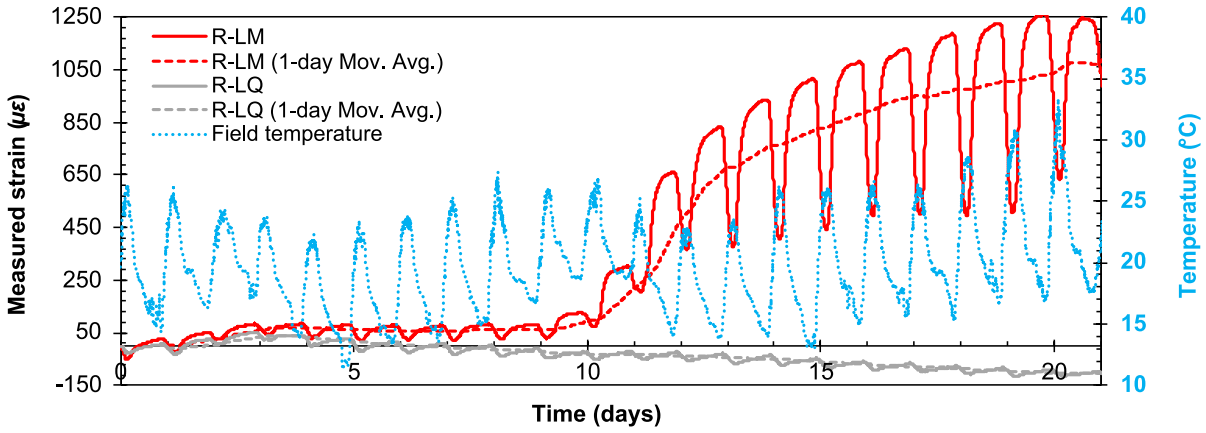

(a) R-LM in PG-200 slab: comparison of actual and 1-day moving average data

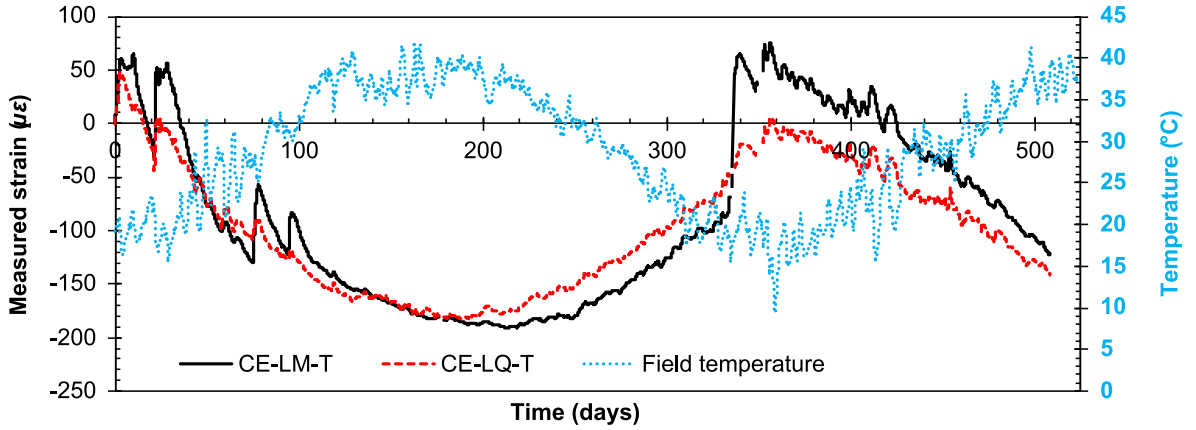

(b) CE-LM-T and CE-LM-B in PG-200 slab (1-day moving average)

Fig. 8. Effect of temperature on strains.

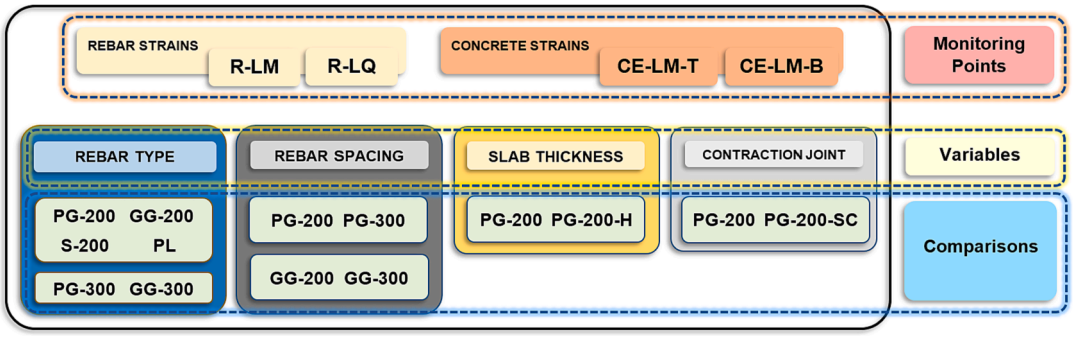

Fig. 9. Sketch showing nomenclatures for monitoring points, variables, and comparisons.

strain than its counterpart with 300 mm spacing. This is not consistent with the notion that a higher reinforcement ratio would lead to lesser strains, with the smaller crack width recorded in the crack maps in Fig. 6 (e and f). It is likely that R-LM in GG-200 was closer to the crack than R-LM in GG-300.

3.3.2. Evolution of rebar strain in the central longitudinal bar at quarter span (R-LQ)

(i) Slabs PG-200, GG-200 and S-200

During early-age, as shown in Fig. 11 (a), strains in all three slabs were identical until the 6th day, after which the curves followed similar paths but with slightly different magnitudes. The measured strains in these slabs at this location were initially tensile at the quarter spans but transitioned to compressive between 7th and 9th days. The compressive strain indicates that no cracks had developed near these sensor locations. As shown in Fig. 11 (b), both GFRP bar-reinforced slabs behaved similarly over the long-term, exhibiting a maximum difference of approximately 40 με. However, the R-LQ of S-200 exhibited a sudden loss of compressive strain on the 112th day, causing the bar to be in tension on the 185th day. This transition can be attributed to the development of a crack in the proximity of the sensor. No further readings could be obtained from the sensor as it malfunctioned after this point.

The long-term curves show that the strains in the GFRP bars at this

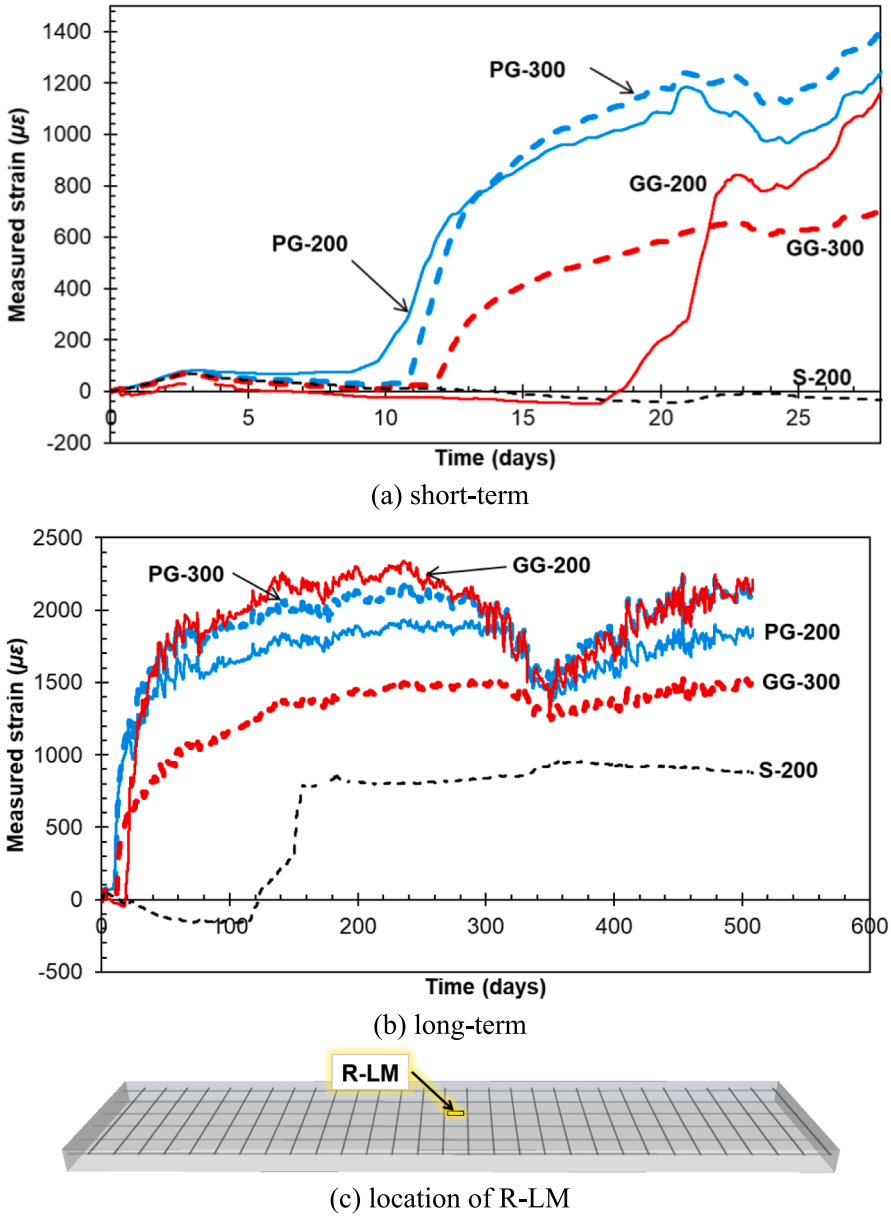

Fig. 10. Effect of rebar types and spacings on the evolution of R-LM.

location increased in compression during the hot summer months and relaxed as the ambient temperature dropped, followed by a slight tension during peak winter, and then returned to compression as the environmental temperature increased. The peak strains in the slabs PG-200, GG-200, and S-200 at the sensor R-LQ were −227 με, −187 με, and −198 με, respectively.

(ii) Slabs PG-300 and GG-300

Soon after the initial swelling of the concrete, which rose until the third day, the strains at R-LQ in both slabs diverged. The peak strain in the longitudinal bar at the quarter-span was −240 με and −312 με in the slabs PG-300 and GG-300, respectively. In the long-term, even at the peak of the summer, none of the sensors recorded tensile strains in the reinforcing bars. The larger strains in GG-300 imply that the sand-coated GFRP bar (GG) had a slightly better bond with concrete in the slab compared to the ribbed GFRP bar (PG).

(iii) Slabs PG-200 and PG-300

The measured strains in PG-200 were generally slightly lower than that in slab PG-300 during the long-term monitoring period, which was probably due to the higher restraint to movement caused by a higher reinforcement ratio. At the peak, the strains at R-LQ in PG-200 and PG-300 were measured to be −227 με and −240 με, respectively.

(iv) Slabs GG-200 and GG-300

Early-age strains were identical in GG-200 and GG-300 until the 6th day, after which the curves split, with compressive strains in GG-300 being significantly higher. No signs of cracking were observed near these sensors, consistent with the crack maps shown in Fig. 6 (e and f). In the long-term, both GFRP bar-reinforced slabs behaved similarly, showing a maximum difference of approximately 125 με. While the R-LQ in GG-300 remained in a state of compression throughout the monitoring period, the strain at R-LQ in GG-200 became tensile for a short

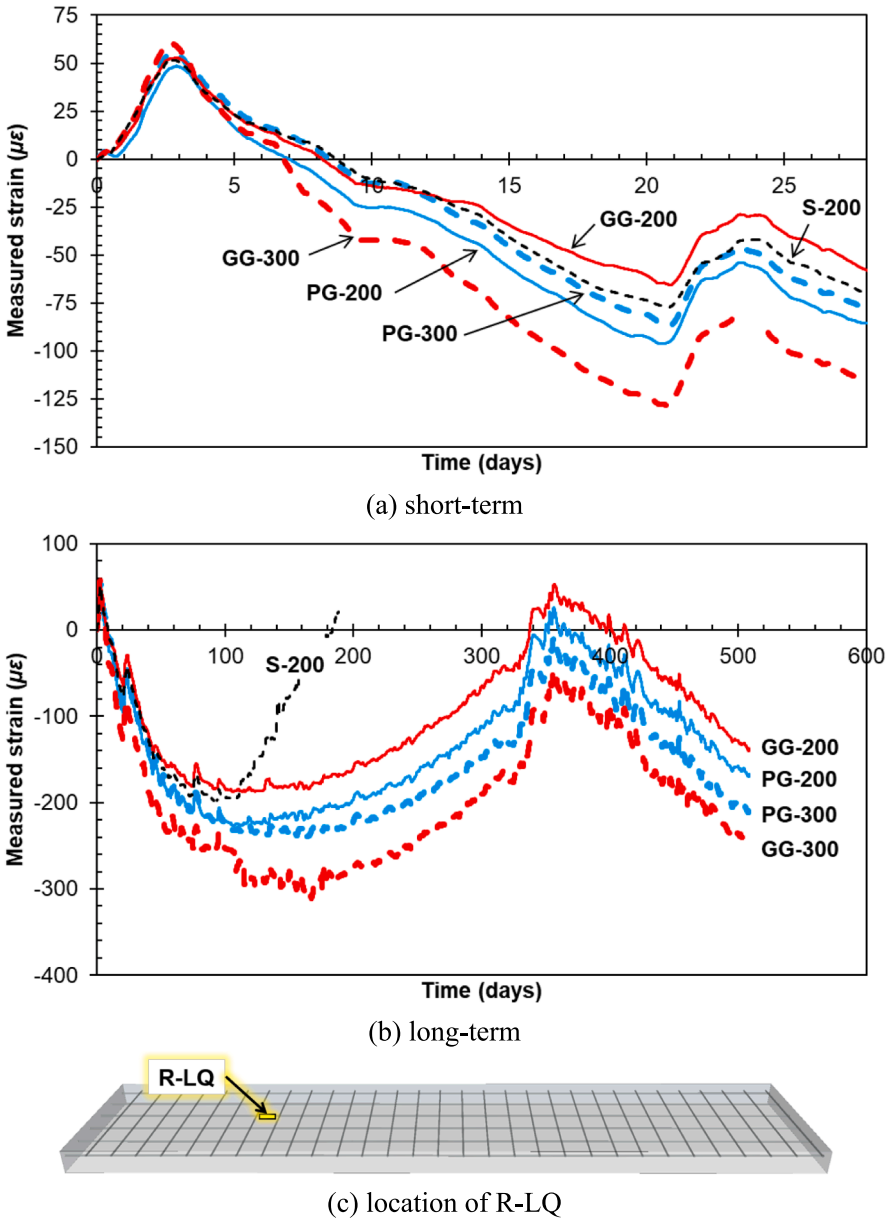

Fig. 11. Effect of rebar types and spacings on the evolution of R-LQ.

time at the peak of winter. The higher strains in GG-300 indicate that the larger reinforcement ratio in GG-200 played an important role in controlling the strains. This reflects a better bond strength in GG bars, as compared to PG bars.

3.3.3. Variation of strain along the longitudinal and transverse bars

The profile of the maximum measured strains in the reinforcing bars along the length of the slab at the longitudinal (R-LM, R-LQ, and R-LE) and transverse bars (R-TM and R-TQ) is shown in Fig. 12 (a) and (b), respectively. The maximum compressive or tensile strains from the long-term field responses of the reinforcing bars were selected for the plots.

3.4. Effect of rebar types and spacings on strain evolution in concrete

3.4.1. Concrete strains at midspan in the longitudinal direction

(i) Slabs PG-200, GG-200, S-200, and PL

Strain gauges embedded in the concrete slab specimens were used to monitor the development of strains in the concrete. Fig. 13 shows the evolution of the concrete strains at mid-span, recorded from strain gauges aligned longitudinally and placed at a depth of 50 mm from the top surface of the concrete specimens (CE-LM-T) and 50 mm above the base of the specimens (CE-LM-B). The concrete strains observed on the slabs-on-ground are the result of the equilibrium between the temperature effects, shrinkage of the concrete, and internal and external restraints such as the embedded reinforcements and the interaction with the subbase. It was found that the strains in the concrete at the level of the reinforcement are slightly larger than the strains in the concrete 50 mm above the base (Fig. 13 (b)). This is because the concrete near the bottom is subjected to a greater restraint at the base of the slab compared to the restraint offered by the reinforcing bars, located at 50 mm from the top surface. From the long-term strain evolution of CE-LM-T and CE-LM-B, the concrete strains in S-200 were the highest among the four slabs compared. The slab S-200 had negative (i.e., compression) peak values of −302 με and −227 με in CE-LM-T and CE-LM-B, respectively, as compared to −191 με and −183 με in PG-200, −160 με and −97 με in GG-200 and −120 με and −220 με in PL slabs. None of the

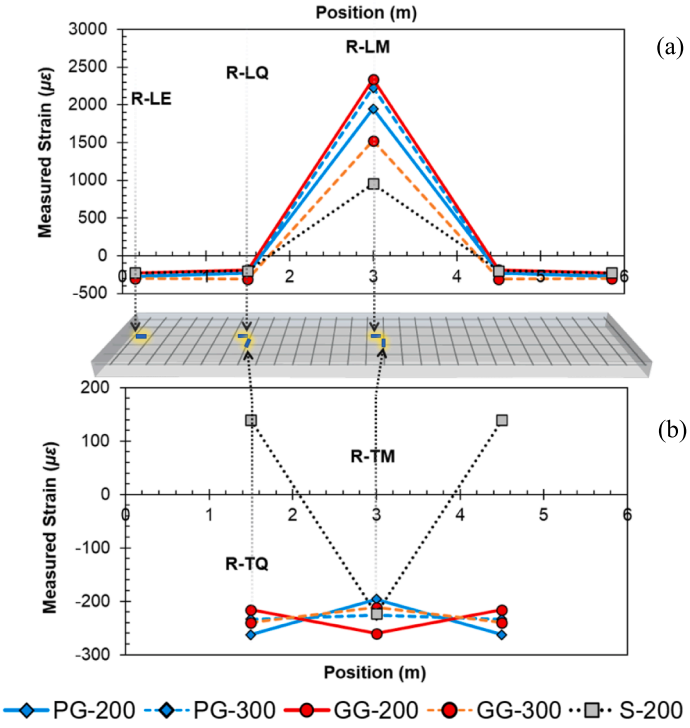

Fig. 12. Summary of peak rebar strain profiles (symmetrized): (a) longitudinal bar (top); and (b) transverse bars (bottom).

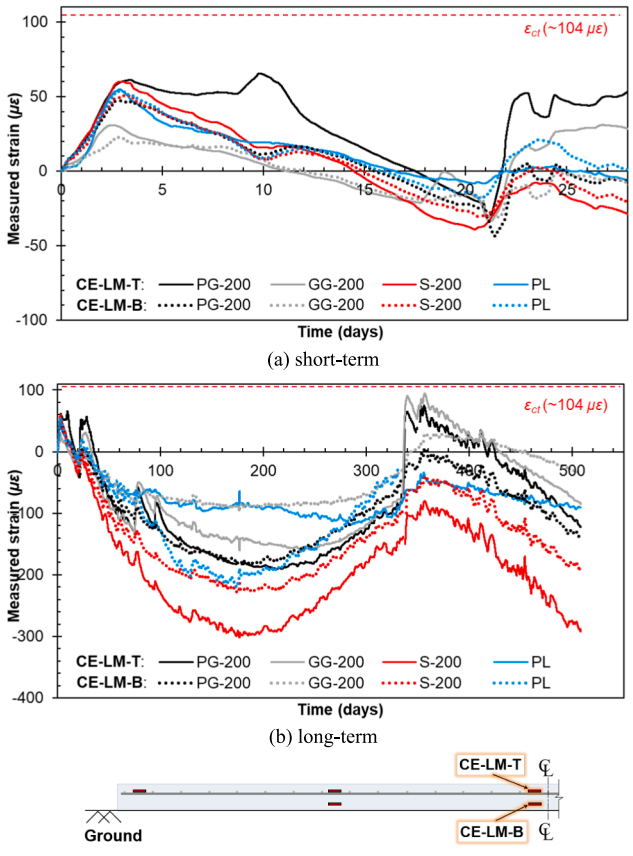

Fig. 13. Effect of rebar type: evolution of CE-LM-T and CE-LM-B in PG-200, GG-200, S-200 and PL slabs.

positive (i.e., tensile) strains in the concrete exceeded the concrete cracking strain, ε_{ct}, which equals + 104 με. The lower negative concrete strains in PG-200 and GG-200 compared to S-200 could be attributed to the fact that these specimens had developed a prominent central crack during the early-age, causing the concrete near the crack, where strain gauges were located, to relax. Also, the lower bond strength between concrete and GFRP bars, as compared to steel [24–26], would have impacted the development of lower strains in concrete, particularly near the location of the drying shrinkage crack.

(ii) Slabs PG-300 and GG-300

Shrinkage of concrete at two depths at the midspan of the slab-on-ground specimens PG-300 and GG-300 are plotted in Fig. 14. CE-LM-T and CE-LM-B exhibited approximately similar behavior up to the first 10 days after casting, indicating that the concrete swelling phenomenon described earlier is independent of the location in the concrete. After this period, when the concrete had gained sufficient strength, a clear distinction in the trajectory of the strain evolution plots could be observed. The strains in the concrete near the top surface of the specimens (CE-LM-T) were significantly higher than the strains near the base (CE-LM-B). This can be attributed to the lower restraint offered by the reinforcing bars as compared to the base, resulting in higher shrinkage rates near the top surface. At the peak of summer, strains of −368 με and −158 με were measured in slab PG-300 in the sensors at CE-LM-T and CE-LM-B, respectively, while strains of −401 με and −186 με were measured in slab GG-300, at the top and bottom, respectively. None of the strains in the concrete surpassed the concrete cracking strain (ε_{ct}), since strain gauges were located away from the cracked locations.

(iii) Slabs PG-200 and PG-300

After the first few days of swelling observed in the concrete, the strains in concrete in the slabs PG-200 and PG-300, remained in a state of compression throughout the monitoring period (Fig. 14 (a)), except for CE-LM-T of PG-200, which changed to positive strain during the

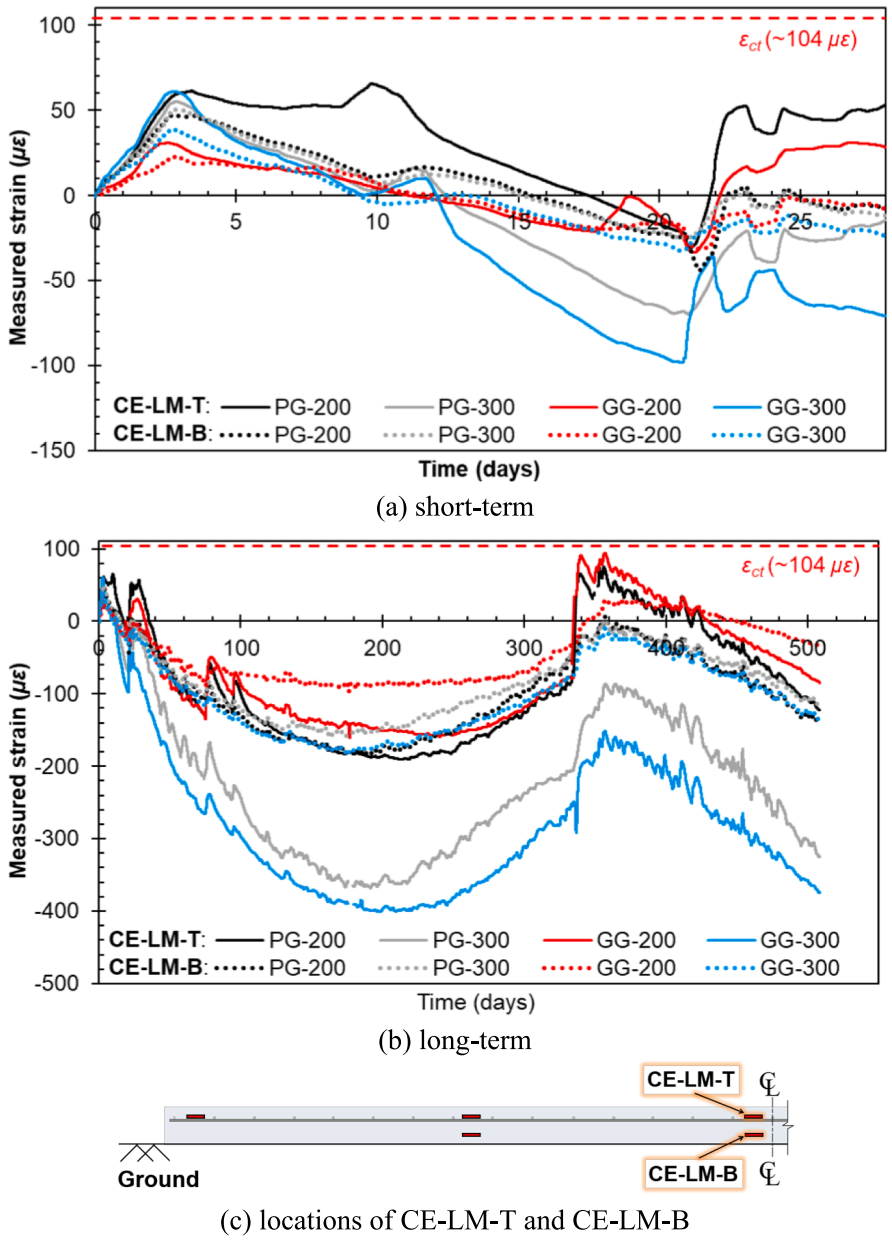

Fig. 14. Effect of rebar spacing: evolution of CE-LM-T and CE-LM-B.

winter peak (Fig. 14 (b)). Although there was a significant difference of 210 με in the measured negative peak strains between CE-LM-T and CE-LM-B in the slab PG-300, the difference between these monitoring points in the slab PG-200 was 8 με only.

(iv) Slabs GG-200 and GG-300

Shrinkage strains in the concrete at two depths at the midspan of the slab-on-ground specimens are plotted in Fig. 14. The sensors at CE-LM-T and CE-LM-B showed almost similar behavior up to the first 10 days after casting. After this period, plots were found to take two distinct paths, depending upon the location of observation, which was consistent with the trends observed for the slabs PG-200 and PG-300. The strain in the concrete near the top of the specimens (CE-LM-T) was notably higher than the strains near the bottom (CE-LM-B). At the peak of summer, the strains in slab GG-200 were recorded to be −160 με and −96 με, respectively, at CE-LM-T and CE-LM-B, while in slab GG-300, the strains were measured to be −401 με and −186 με. The concrete strains recorded at the quarter-span (CE-LQ-T and CE-LQ-B) also showed a similar path of evolution.

3.4.2. *Strain profile along the length and across the depth of slabs*

Fig. 15 shows the profile of the peak strains developed in concrete at the midpoint, quarter point, and the ends of the slab at 50 mm below the top surface (CE-LM-T, CE-LQ-T, and CE-LE) and at 50 mm above the base (CE-LM-B and CE-LQ-B).

3.5. *Effect of slab thickness on strains*

The influence of slab thickness was investigated by comparing the development of strains in the 100 mm-thick slab (PG-200-H) and the 200 mm-thick slab (PG-200). The specimen PG-200-H was made with ribbed GFRP bars spaced 200 mm c/c in both directions, and the reinforcement cage was placed at mid-depth. The strain on main GFRP bars at midspan in both PG-200 and PG-200-H showed very similar readings. The sensor R-LM in both slabs detected the occurrence of drying

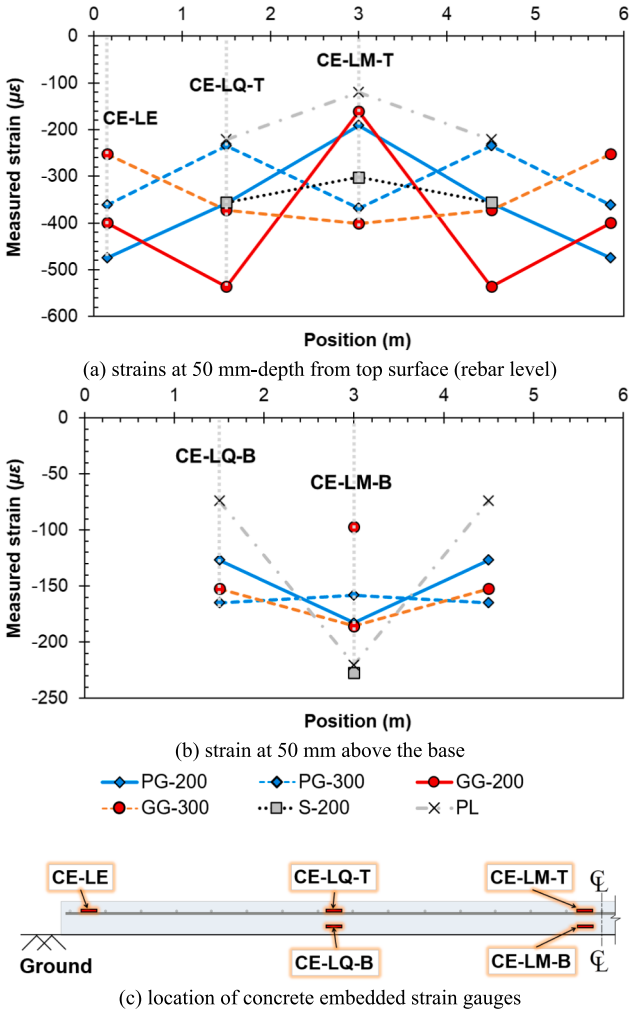

(a) strains at 50 mm-depth from top surface (rebar level)

(b) strain at 50 mm above the base

(c) location of concrete embedded strain gauges

Fig. 15. Summary of peak concrete strain profiles (symmetrized).

shrinkage cracks on the 10th day after casting (Fig. 16 (a)). The average crack width measured in PG-200 and PG-200-H was 0.62 mm and 0.61 mm, respectively. The long-term monitoring results show that the strain (Fig. 16 (b)) in slab PG-200-H was only marginally lower than slab PG-200.

The strain development curves on GFRP bars at the quarter point (R-LQ) and in the transverse bar at mid-span (R-TM) in both 100 mm- and 200 mm-thick slabs are shown in Fig. 16 (c and d). At the quarter point (R-LQ), the evolution of strains in the slabs PG-200 and PG-200-H followed closely during short and long-term observations. However, in the transverse bars (R-TM), a notable difference in the strain response was observed, particularly evident in the long-term monitoring. The peak strain in PG-200-H (-341 $\mu\varepsilon$) was 73% higher than that of the strains in PG-200 (-196 $\mu\varepsilon$). Fig. 17 (a) shows the profile of the peak strains developed at the monitored points of the longitudinal bar, while Fig. 17 (b) shows the strain profile in the transverse bars.

The effect of slab thickness on concrete strains at the midspan of the specimens is shown in Fig. 18 (a and b). It can be seen from the figure that the strain at midspan (CE-LM-T) in slab PG-200 continued to exhibit negative strains despite the development of a full-depth drying shrinkage crack in the vicinity of the sensor. The sensor CE-LM-T in PG-200-H abruptly changed from negative strains to large positive strains of over 2,500 $\mu\varepsilon$, as shown in Fig. 18 (b). This indicates the formation of a crack intercepting the strain gauge [13]. The measured strain in concrete in PG-200-H crossed the cracking limit (ε_{ct}) of 104 $\mu\varepsilon$ on the 38th day after. Fig. 19 (a) shows the profile of the peak concrete strain developed at the points 50 mm below the top surface, CE-LM-T, CE-LQ-T, and CE-LE.

3.6. *Effect of the saw-cut contraction joint at midspan of slab*

The use of contraction joints in slabs-on-ground is a common practice to avoid the development of cracks in non-uniform patterns. In the Jazan flood mitigation channel, these joints were introduced at intervals of 6 m center-to-center in both directions [18]. The introduction of a predetermined crack would force the concrete to crack at the plane in which the joint was created, owing to its reduced cross-sectional area. In practice, flexible sealants are used to fill the gap to prevent the ingress of water and chemicals [27].

Upon analyzing the strains at the mid-span of the longitudinal bars, it is apparent that sensors at R-LM in both PG-200 and PG-200-SC captured the commencement of drying shrinkage cracks on the 10th day, according to Fig. 16 (a and b). The strain evolutions of R-LMs further along the monitoring duration were very similar, as expected, with the peak strains being 1,854 $\mu\varepsilon$ and 1,950 $\mu\varepsilon$ in PG-200-SC and PG-200, respectively. Strains in rebars in other locations of slabs, such as R-LE and R-TQ, too were similar to each other in terms of trends in the trajectory of the curves at R-LQ (Fig. 16 (c and d)). The profiles of the highest strains developed at the points on the longitudinal bar, R-LM, R-LQ, and R-LE, are shown in Fig. 17 (a), while that of transverse bars R-TM and R-TQ are shown in Fig. 17 (b). The effect of introducing a saw-cut contraction joint on concrete strains at the mid-span of specimens was analyzed.

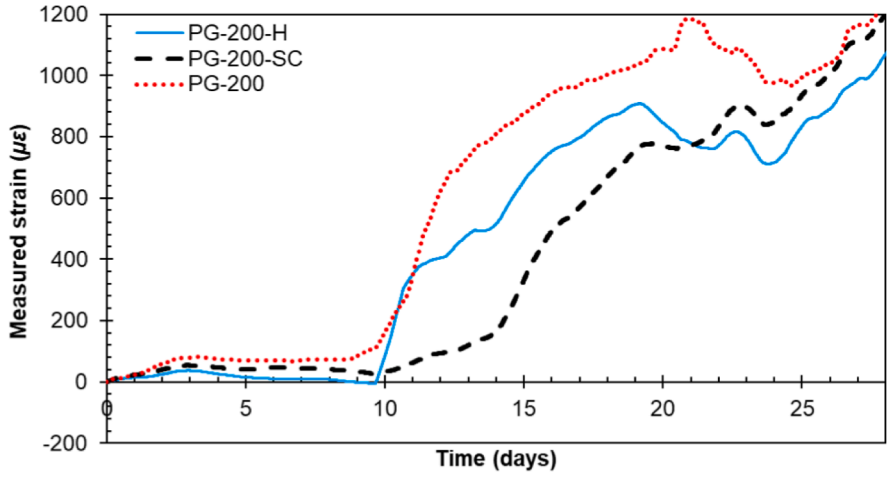

(a) R-LM (short-term)

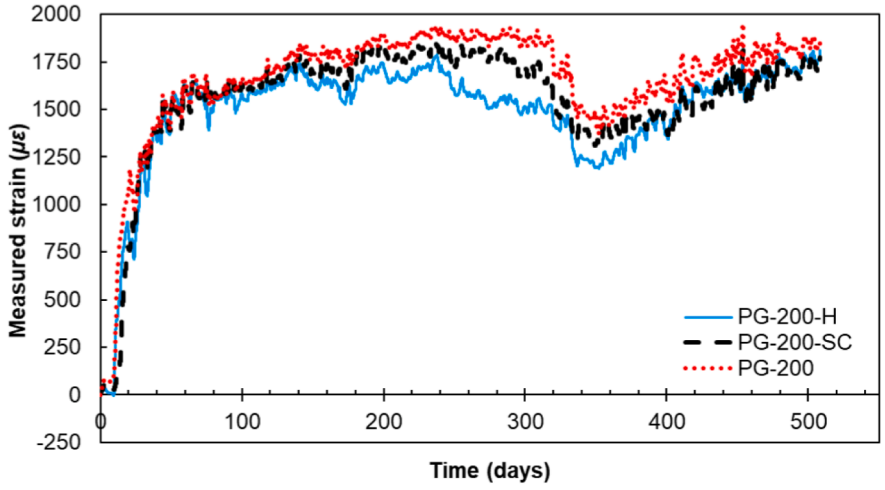

(b) R-LM (long-term)

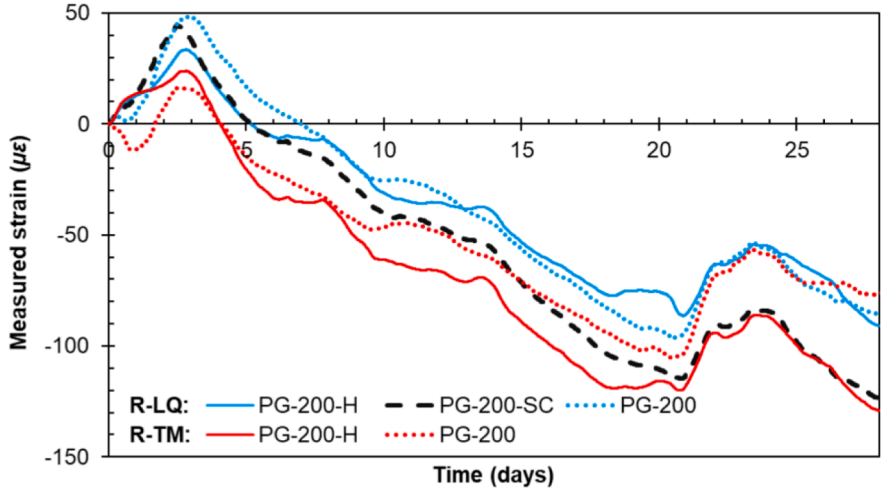

(c) R-LQ and R-TM (short-term)

Fig. 16. Rebar strains in PG-200-H, PG-200-SC and PG-200 slabs.

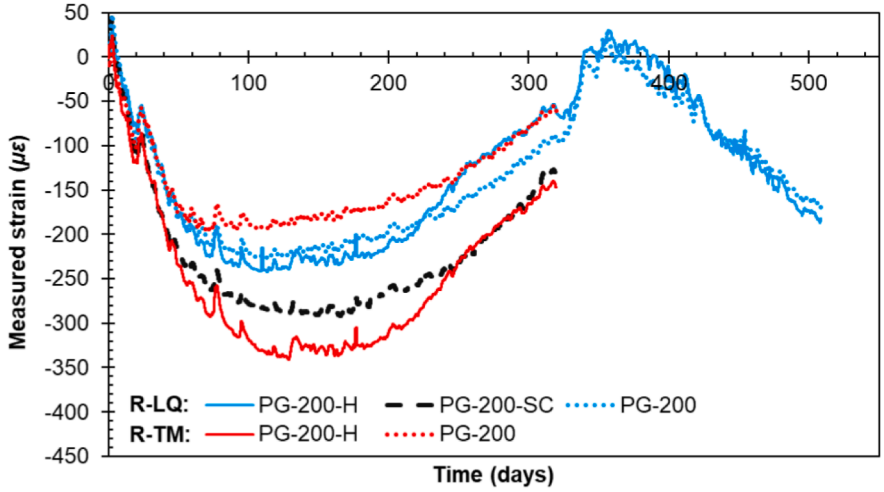

(d) R-LQ and R-TM (long-term)

Fig. 16. (*continued*).

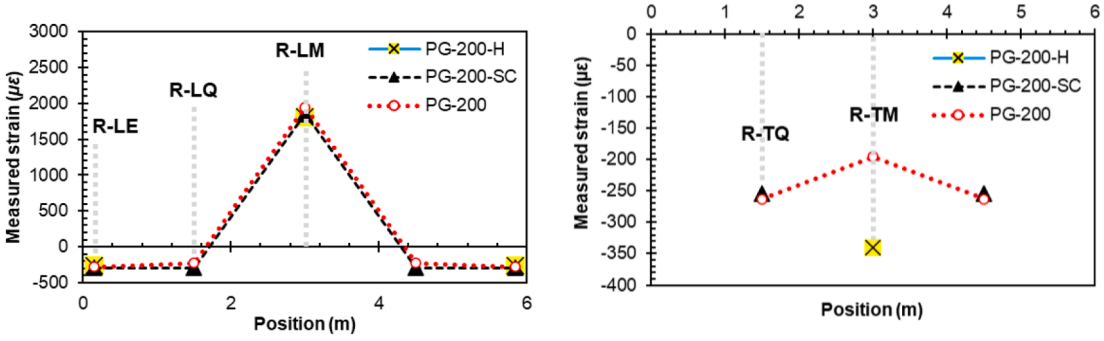

(a) rebar: longitudinal bar (b) rebar: transverse bars

Fig. 17. Peak rebar strain profiles in PG-200-H, PG-200-SC and PG-200 slabs.

Concrete strains at CE-LM-T in PG-200-SC abruptly changed from negative strains to large positive strains of approximately 6,900 με, as shown in Fig. 18 (a and b), which suggests that a drying shrinkage crack intercepted the embedded concrete strain gauge, as also observed in PG-200-H [13]. The strains at R-LM in PG-200-SC surpassed the concrete cracking limit (ε_{ct}) of 104 με on the 23rd day after casting.

Shrinkage in concrete taking place at two depths (CE-LQ-T and CE-LQ-B) at the quarter-span of the slab-on-ground specimens, PG-200 and PG-200-SC, are plotted in Fig. 18 (c and d). Sensors at CE-LM-T and CE-LM-B exhibited approximately similar behavior up to the first 3 days after the casting, beyond which plots were found to take different paths. As observed in previous comparisons, concrete strains near the top surface of the specimens (CE-LQ-T) were higher than those near the base (CE-LQ-B). At the peak of summer, in PG-200, CE-LQ-T and CE-LQ-B were recorded to be −357 με and −127 με, respectively, while in PG-200-SC, CE-LQ-T and CE-LQ-B were recorded to be −278 με and −244 με. Fig. 19 (a) shows the profile of the peak concrete strains developed at the points 50 mm below the top surface, CE-LM-T, CE-LQ-T, and CE-LE, and Fig. 19 (b) shows the peak strains at CE-LM-B and CE-LQ-B.

4. Conclusions

A detailed experimental work was conducted to assess the field performance of GFRP bar-reinforced concrete slabs-on-ground subjected to environmental exposure for 525 days. A total of eight large-scale reinforced slabs-on-ground were cast during the cooler days of the year with a 1-day average temperature of 19.2 °C, and RH of 66.2%. At the peak of summer, the average temperature and RH changed to 41.7 °C and 12.8%, respectively, while at the peak of winter, the temperature and RH were recorded to be 9.5 °C and 87.7%, respectively. This huge variation in ambient conditions was found to have a profound impact on the evolution of strains in GFRP bars as well as concrete. The study focused on the effect of design parameters such as reinforcement type and spacing, slab thickness, and the presence of saw-cut contraction joint on the nature of concrete crack development and the evolution of rebar and concrete strain. Based on the findings of the experimental program, the following conclusions were drawn:

- The crack mapping of the eight slabs revealed that a central prominent drying shrinkage crack developed in all GFRP bar-reinforced slabs. The crack widths in the six GFRP bar-reinforced slabs were within ACI 440.1R-15 and AASHTO LFRD code limits of 0.7 mm. The central cracks were developed in both ribbed and sand-coated GFRP bars. The rebar spacing of 200 mm (PG-200) and 300 mm (PG-300) did not have any significant impact on the crack width. However, for slabs reinforced with sand-coated GFRP (GG) bars, the slab with 300 mm spacing (GG-300) exhibited a crack width 29.4% larger than the slab with 200 mm spacing c/c (GG-200). The steel-reinforced slab (S-200) did not develop a central crack, unlike the other GFRP bar-reinforced slabs.
- Cracks in PG-200, PG-300, GG-200, PG-200-H, and PG-200-SC developed within the same timespan varying from 9 to 12 days as

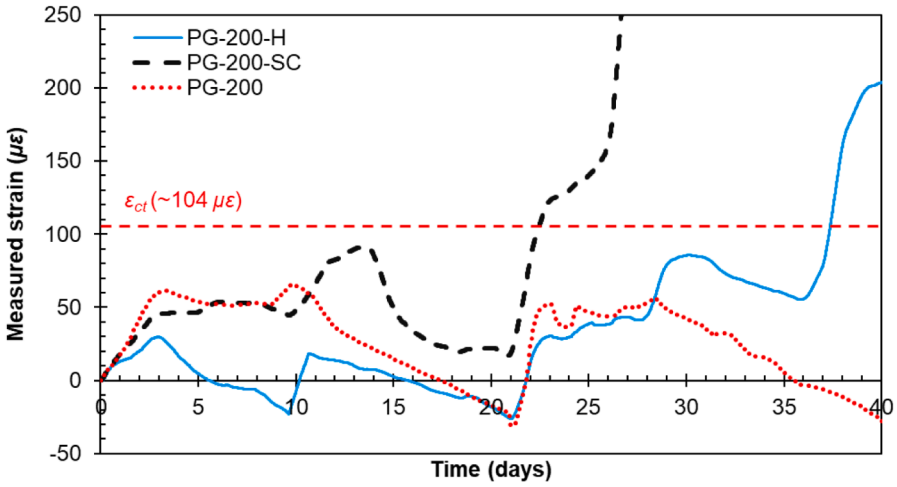

(a) CE-LM-T (short-term)

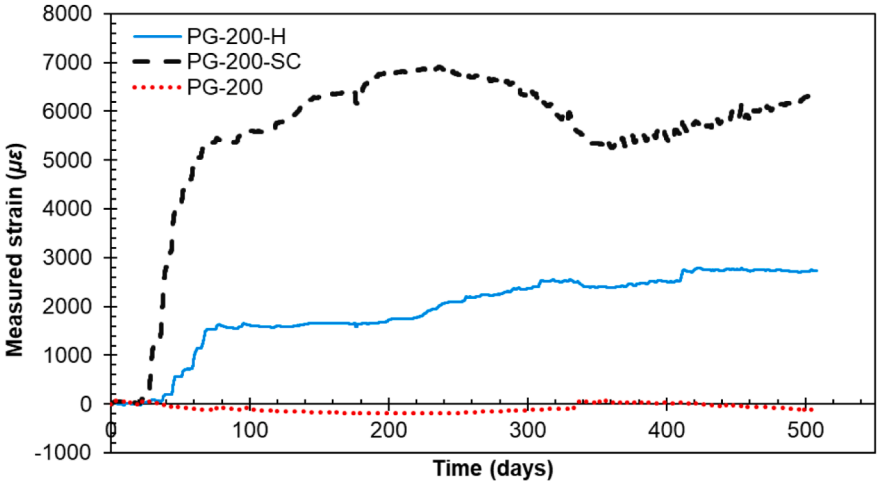

(b) CE-LM-T (long-term)

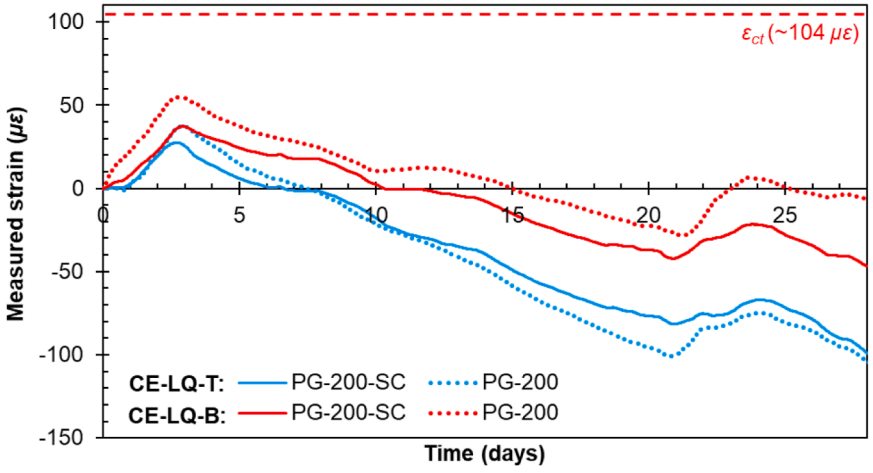

(c) CE-LQ-T and CE-LQ-B (short-term)

Fig. 18. Concrete strains in PG-200-H, PG-200-SC and PG-200 slabs.

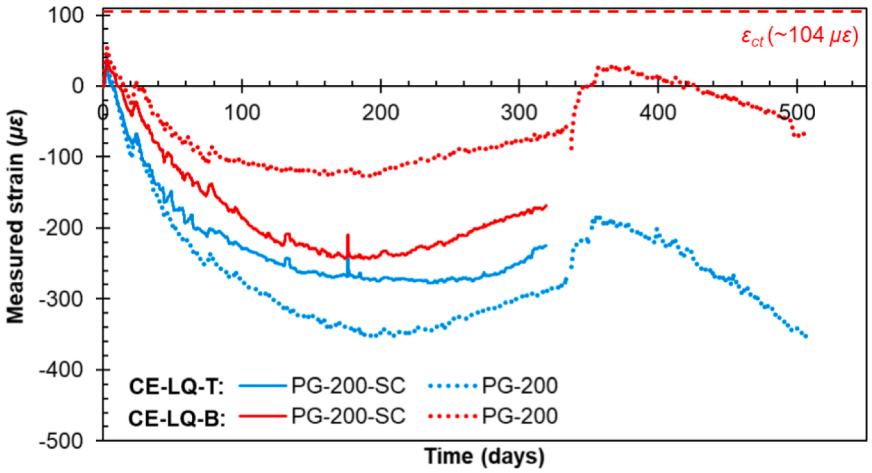

(d) CE-LQ-T and CE-LQ-B (short-term)

Fig. 18. (*continued*).

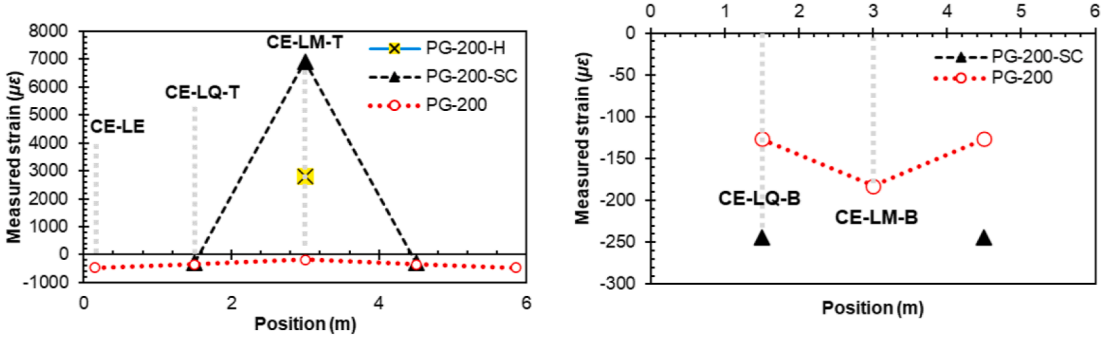

(a) concrete: at rebar level (50 mm from top surface) (b) concrete: 50 mm above base

Fig. 19. Peak concrete strain profiles in PG-200-H, PG-200-SC, and PG-200 slabs.

observed from sensors data, although there was a lag of 2 to 4 days when the cracks were visually observed on the slab. However, the sand-coated GFRP (GG) bar-reinforced slab with 200 mm spacing, GG-200 cracked at 18 days and had a significantly low crack width.

- Rebar strains were found to vary significantly depending on their location with respect to the location of the drying shrinkage crack. In the GFRP bar-reinforced slabs, rebars located near the central drying shrinkage crack began to sustain tensile strains soon after the crack was developed. Calculated tensile stresses of 94.4 MPa, 107.8 MPa, 102.7 MPa, and 66.9 MPa were developed in the longitudinal rebars near the central drying shrinkage cracks in PG-200, PG-300, GG-200, and GG-300, respectively.
- The measured strains were found to vary significantly across the depth in the slabs-on-ground. Due to the higher restraints at the interface between the base of the concrete slabs and the lean concrete subbase, the measured strains near the base of the specimens were lower than that near the top surface (at rebar level), at mid- as well as quarter spans. In both PG-200 and GG-200 slabs, the measured strains at rebar level at quarter-spans (CE-LQ-T) were higher than mid-spans (CE-LM-T) by 87% and 234%, respectively. However, in the 300 mm-spacing slabs, measured strains CE-LQ-T as compared to CE-LM-T, were lower by 36% and 7%, in PG-300 and GG-300, respectively.
- The times of development of the central drying shrinkage crack as well as the observed crack width were similar in the 200 mm-thick slab, PG-200, and the 100 mm-thick slab, PG-200-H. Also, the peak calculated tensile stresses in the longitudinal rebars at midspan (R-LM) were similar, with 87.5 MPa and 94.4 MPa in PG-200-H and PG-200 slabs, respectively, as in the case of longitudinal rebar strains at quarter spans with −242 με and −227 με. It was observed that reducing the thickness of the slab did not adversely affect the performance of the slabs-on-ground, in terms of cracking and strain evolution.
- The slab specimen with the saw-cut contraction joint (PG-200-SC) and reference slab PG-200 developed the central cracks at approximately the same time. However, the average crack width in PG-200-SC below the saw-cut was 0.43 mm, while that on the top surface of PG-200 was 0.62 mm. Cracking in PG-200-SC developed exactly in the plane of the saw-cut, as anticipated, unlike the case of PG-200, in which the location was random. Besides being more aesthetically pleasing, PG-200-SC allows for the effective application of sealants to prevent the seepage of corrosive chemicals to reach the rebars. The evolution of rebar and concrete strains in PG-200-SC was comparable with PG-200. Peak tensile stresses in the longitudinal rebars at mid-span (R-LM) were 89.7 MPa and 94.4 MPa in PG-200-SC and PG-200, respectively. In the same bar, at quarter-span (R-LQ), however, PG-200-SC recorded 29% more negative strains. On the other hand, PG-200-SC exhibited 22.1% lower strains at CE-LQ-T and 92.5% higher negative strains at CE-LQ-B, respectively, as compared to PG-200.

CRediT authorship contribution statement

Mohammed Fasil: Conceptualization, Formal analysis,

Investigation, Software, Validation, Visualization, Writing – original draft. **Muhammad Kalimur Rahman:** Conceptualization, Formal analysis, Investigation, Software, Validation, Visualization, Writing – original draft. **Mesfer M. Al-Zahrani:** Funding acquisition, Investigation, Methodology, Project administration, Supervision, Writing – review & editing. **Antonio Nanni:** Conceptualization, Visualization, Writing – review & editing. **Mohammed A. Al-Osta:** Conceptualization, Formal analysis, Investigation, Software, Validation, Visualization, Writing – original draft. **Sami A. Al-Ghamdi:** Funding acquisition, Project administration, Writing – review & editing. **Mohammed Al Mehthel:** Conceptualization, Formal analysis, Investigation, Software, Validation, Visualization, Writing – original draft.

Declaration of Competing Interest

The authors declare that they have no known competing financial interests or personal relationships that could have appeared to influence the work reported in this paper.

Data availability

The authors do not have permission to share data.

Acknowledgements

The authors gratefully acknowledge the financial support provided by Saudi Aramco under contract No. 6600011900 for this research. The authors would like to thank the Interdisciplinary Research Center for Construction and Building Materials (IRC-CBM), Applied Research Center for Metrology, Standards and Testing (ARC-MST), and the Civil and Environmental Engineering (CEE) Department at the King Fahd University of Petroleum and Minerals (KFUPM), Saudi Arabia for providing all the necessary support for conducting the research. The authors acknowledge the contribution of Mohammed Ibrahim, Mohammed Salihu Barry, Syed M. Shaahid, and Syed K. Najamuddin for their contributions in the study.

References

[1] Larosche CJ. 3 - Types and causes of cracking in concrete structures. In: Delatte N, editor. Failure, Distress and Repair of Concrete Structures, Woodhead Publishing; 2009, p. 57–83. https://doi.org/10.1533/9781845697037.1.57.
[2] TRB. Control of Cracking in Concrete: State of the Art. Washington, D.C.: Transportation Research Board; 2006. https://doi.org/10.17226/23231.
[3] R. Frosch, D. Blackman, R. Radabaugh, Investigation of Bridge Deck Cracking in Various Bridge Superstructure Systems, Purdue University, West Lafayette, IN, 2003, https://doi.org/10.5703/1288284313257.
[4] S. Shadravan, C. Ramseyer, T.-H.-K. Kang, A long term restrained shrinkage study of concrete slabs on ground, Eng. Struct. 102 (2015) 258–265, https://doi.org/10.1016/j.engstruct.2015.08.018.
[5] X. Zhou, W. Dong, O. Oladiran, Experimental and Numerical Assessment of Restrained Shrinkage Cracking of Concrete Using Elliptical Ring Specimens, J. Mater. Civ. Eng. 26 (2014) 04014087, https://doi.org/10.1061/(ASCE)MT.1943-5533.0001001.
[6] A.S.A. Al-Hedad, M. Zhang, M.N.S. Hadi, Influence of Geogrid Reinforcement on the Drying Shrinkage of High-Strength Concrete Pavements, J. Transp. Eng., Part B: Pavements 146 (2020) 04020032, https://doi.org/10.1061/JPEODX.0000184.
[7] K. Raoufi, M. Pour-Ghaz, A. Poursaee, J. Weiss, Restrained Shrinkage Cracking in Concrete Elements: Role of Substrate Bond on Crack Development, J. Mater. Civ. Eng. 23 (2011) 895–902, https://doi.org/10.1061/(ASCE)MT.1943-5533.0000247.
[8] A. Ghatefar, E. El-Salakawy, M. Bassuoni, Effect of Reinforcement Ratio on Transverse Early-Age Cracking of GFRP-RC Bridge Deck Slabs, J. Compos. Constr. 18 (2014) 04014018, https://doi.org/10.1061/(ASCE)CC.1943-5614.0000479.
[9] ACI Committee 440. ACI CODE 440.11-22: Building Code Requirements for Structural Concrete Reinforced with Glass Fiber-Reinforced Polymer (GFRP) Bars-Code and Commentary. 1st printing. Farmington Hills, MI: American Concrete Institute (ACI); 2022.
[10] A. Ghatefar, E. El-Salakawy, M.T. Bassuoni, Early-age restrained shrinkage cracking of GFRP-RC bridge deck slabs: Effect of environmental conditions, Cem. Concr. Compos. 64 (2015) 62–73, https://doi.org/10.1016/j.cemconcomp.2015.07.010.
[11] CSA. CAN/CSA-S6-06: Canadian Highway Bridge Design Code. CSA Group; 2006.
[12] B. Shafei, B. Phares, D. Saini, Field Investigation of Bridge Deck Reinforced with Glass Fiber Reinforced Polymer (GFRP) Rebar, Local Road Research Board, Minnesota Department of Transportation, Minnesota, USA, 2020.
[13] E. Cuelho, P. Smolenski, J. Stephens, J. Johnson, Evaluating concrete bridge deck performance, Montana State University and State of Montana Department of Transportation, Montana, 2004.
[14] C.P. Pantelides, K.M. Holden, J. Ries, Health monitoring of precast bridge deck panels reinforced with glass fiber reinforced polymer bars (GFRP), Utah Department of Transportation, Utah, USA, 2012.
[15] D. Kušnírová, S. Priganc, Deflection of concrete slabs with GFRP reinforcement caused by shrinkage, Selected Sci. Papers – J. Civil Eng. 14 (2019) 113–118, https://doi.org/10.1515/sspjce-2019-0012.
[16] R. Sonnenschein, N. Gazovicova, J. Bilcik, Experimental and Numerical Study of Early-age Cracking of Concrete Slabs Reinforced with Steel and GFRP Bars, ACT 19 (2021) 1197–1211, https://doi.org/10.3151/jact.19.1197.
[17] ACI. ACI 440.1R-15: Guide for the design and construction of structural concrete reinforced with fiber-reinforced polymer (FRP) bars. 1st printing. Farmington Hills, MI: American Concrete Institute; 2015.
[18] E.A.V. Salan, M.K. Rahman, S. Al-Ghamdi, J. Sakr, M.M. Al-Zahrani, A. Nanni, A Monumental Flood Mitigation Channel in Saudi Arabia, CI 43 (2021) 33–41.
[19] G. Gardiner, Composite Reinforcing Bars for Future Infrastructure, CI 43 (2021) 23–26.
[20] B. Kucharczyková, L. Topolář, P. Daněk, D. Kocáb, P. Misák, Comprehensive Testing Techniques for the Measurement of Shrinkage and Structural Changes of Fine-Grained Cement-Based Composites during Ageing, Adv. Mater. Sci. Eng. 2017 (2017) 1–10, https://doi.org/10.1155/2017/3832072.
[21] A. Bentur, Early age cracking in cementitious systems: report of RILEM Technical committee 181-EAS, Early age shrinkage induced stresses and cracking in cementitious systems, RILEM publications, Bagneux, 2003.
[22] E. Marušić, N. Štirmer, Autogenous Shrinkage and Expansion Related to Compressive Strength and Concrete Composition, ACT 14 (2016) 489–501, https://doi.org/10.3151/jact.14.489.
[23] B. Kucharczyková, P. Daněk, D. Kocáb, P. Misák, Experimental Analysis on Shrinkage and Swelling in Ordinary Concrete, Adv. Mater. Sci. Eng. 2017 (2017) e3027301, https://doi.org/10.1155/2017/3027301.
[24] R. Okelo, R.L. Yuan, Bond Strength of Fiber Reinforced Polymer Rebars in Normal Strength Concrete, J. Compos. Constr. 9 (2005) 203–213, https://doi.org/10.1061/(ASCE)1090-0268(2005)9:3(203).
[25] Z. Achillides, K. Pilakoutas, Bond Behavior of Fiber Reinforced Polymer Bars under Direct Pullout Conditions, J. Compos. Constr. 8 (2004) 173–181, https://doi.org/10.1061/(ASCE)1090-0268(2004)8:2(173).
[26] Q. Hao, Y. Wang, Z. Zhang, J. Ou, Bond strength improvement of GFRP rebars with different rib geometries, J Zhejiang Univ - Sci A 8 (2007) 1356–1365, https://doi.org/10.1631/jzus.2007.A1356.
[27] J. Kim, D. Zollinger, Effects of Shape and Bond Strength on Adhesive Failure of Joint Sealants, Transp. Res. Rec. 2675 (2021) 203–212, https://doi.org/10.1177/0361198120962095.
[28] AASHTO. AASHTO LRFD Bridge. Design Guide Specifications for GFRP-Reinforced Concrete, The American Association of State Highway and Transportation Officials, Washington, D.C, 2018.